

# **In-situ TEM study of Kr ion irradiation tolerance of SiFeOC nanocomposite**

Kathy Lu\*, Sanjay Singh

Department of Materials Science and Engineering, Virginia Tech, Blacksburg, VA, 24061,  
USA

\*Corresponding author: [klu@vt.edu](mailto:klu@vt.edu)

## **Abstract**

In this work, ion irradiation of polymer derived SiFeOC nanocomposite was carried out using 1.2 MeV Kr ions at room temperature and 600°C. The starting composite was composed of Fe<sub>3</sub>Si, SiC, SiOC, SiO<sub>2</sub>, and graphitic C. In-situ TEM investigations show uniform distribution of nano-crystalline Fe<sub>3</sub>Si and SiC phases in the amorphous SiOC matrix. During ion irradiation, the SiOC bulk microstructure and interfaces between Fe<sub>3</sub>Si or SiC crystallites and the SiOC matrix remain defect-free and demonstrate outstanding ion irradiation resistance. At room temperature, the crystalline domains are stable up to 2 dpa. At 600°C, Fe<sub>3</sub>Si crystallites are more stable than SiC; SiC crystallites are stable up to 4 dpa while the Fe<sub>3</sub>Si crystallites are stable up to 10 dpa. These crystallites also coalesce and amorphize simultaneously during ion irradiation. The exceptional tolerance to defect formation and irradiation of the SiFeOC nanocomposite provides important guidance to developing irradiation resistant fuels for advanced gas cooled reactors.

**Keywords:** Ion irradiation; In-situ transmission electron microscopy; Temperature effect; Defect sink site; Crystallite amorphization

## 1. Introduction

To extend the operating life of existing nuclear reactors and design irradiation-tolerant fuels for advanced nuclear reactors, new irradiation resistant materials are needed [1, 2]. Recent investigations revealed that defect sink sites, such as grain boundaries and interfaces, are effective to resist the irradiation damage and increase irradiation tolerance [3-5]. Studies carried out on materials comprised of nanoscopic metallic interfaces, including Cu/Nb [6], Cu/V [7, 8], and Fe/W [9], revealed that nanoscale interfaces (defect sinks) promote the recombination of defects and suppress void/bubble formation [3].

Polymer-derived SiOC nanocomposites are known for their resiliency to irradiation damages [3] due to fluctuations in their free volume or local bonding topology [10, 11]. Simulations show that defect sink site concentration is proportional to the amount of free volumes formed and these free volumes are often in excess in SiOC nanocomposites [11]. Previous studies reported that SiOCs do not undergo swelling either at room temperature or at 600°C upon irradiation with He ions up to 20 displacement per atoms (dpa) [12, 13]. However, such studies were mainly conducted on sputtered thin films instead of bulk SiOC samples even though the latter are typically needed for nuclear applications. Also, previous studies are often on SiOC systems without SiC formation [14-17]. The ion irradiation effect on nanocrystallite evolution, especially SiC vs. other crystallites in SiOC-based composites, has not been well understood.

From a different perspective, SiC nanodomains are in the single nanometer range in the SiOC matrix [18-23]. To increase the  $\beta$ -SiC and SiOC interface, one viable approach is to increase the amount of SiC formed. Recent studies revealed that Fe catalyst facilitates the formation of SiC through intermediate  $\text{Fe}_3\text{Si}$  [24-29]. Even though the facilitation of SiC formation is through a series of intermediate reactions and different from a classical catalyst, such as Pt, the acceleration of SiC formation is clear. These nanodomains ( $\beta$ -SiC,  $\text{Fe}_3\text{Si}$ , and

graphitic C) may act as defect sink sites during ion irradiation. Therefore, synthesizing new SiOC-based systems and further understanding ion irradiation effect on these new SiOC materials are highly desired in the development of accident tolerant fuels [30]. SiOC/crystalline Fe multilayer thin films [15, 31] have been reported to annihilate point defects generated during irradiation through crystalline/amorphous interfaces and Fe grain boundaries. Fe and amorphous SiOC ceramic not only exhibit exceptional, homogeneous plasticity at room temperature but also retain high strength and good irradiation tolerance [32]. Even SiOC dispersion strengthened steel shows that the SiOC/steel interface can be an effective sink for the annihilation of irradiation defects [33].

In addition, most of the ion irradiation studies carried out on SiOCs were dedicated to light elements, mainly He [11, 12, 34]. It is well known that the damage density created by heavy ions is different from that of light elements [15, 35]. Irradiation using heavy elements, such as Kr ions, might result in the formation of metastable phases or enhanced stability of nanophases in the SiOC matrix. Light ions often create loosely distributed cascades with scattered defects while heavy ions create dense cascade damages [35]. However, studies using heavy ions are scant [15, 36]. Recently, SiOC films were irradiated with 3.5 MeV Fe ions at room temperature with damage levels of 10, 20, and 50 dpa [37]. Irradiation up to 10 and 20 dpa resulted in phase separation to amorphous SiO<sub>2</sub> and C clusters while irradiation to 50 dpa led to conversion of sp<sup>2</sup> C to sp<sup>3</sup> C [37]. No formation of cracks, embrittlement, or layering was observed even though the 20 dpa samples showed enhanced hardness [37]. This means that nanodomain interfaces and the SiOC matrix itself have superior resistance to irradiation induced damages [37, 38]. These nanodomain interfaces coupled with the SiOC matrix act as defect sink sites and enhance the mechanical behaviors [15, 38].

Ex-situ transmission electron microscopy (TEM) study of irradiated samples can only observe microstructural changes before and after irradiation. However, real-time information

is required for in-depth understanding of microstructure evolution. Further, ex-situ TEM is time consuming when a series of ion irradiation experiments must be conducted, without the possibilities to observe the microstructure changes at the same locations or allow accurate capture of certain continuous event(s) at different stages of irradiation. In-situ TEM under ion irradiation, especially at different temperatures, would shed more light in the microstructural evolution. Recently, in-situ TEM was used to explore real-time atomic scale charging and discharge processes in a battery [39]. It led to fundamental understanding in swelling and cracking of SnO<sub>2</sub> nanowires [39]. Similarly, in-situ irradiation experiments was used to evaluate the stability of Y-Ti-O nano-precipitates in ferritic-martensitic steels [40]. Y-Ti-O nanoclusters of 5 nm size were stable up to 45 dpa when irradiated using 150 keV Fe<sup>+</sup> at 500°C [40]. In-situ TEM study on UO<sub>2</sub> confirmed the rapid formation of Xe bubbles under 390 keV Xe<sup>3+</sup> irradiation. These kinds of events cannot be captured from ex-situ TEM studies.

In this study, Kr ion irradiation was performed on a newly synthesized SiFeOC ceramic both at room temperature and at 600°C using in-situ TEM. This SiFeOC composite is different from the SiOC/crystalline Fe multilayer thin films discussed earlier in that it is in a bulk format with a different Fe-containing phase: Fe<sub>3</sub>Si. Ion irradiation effect on the microstructural evolution of SiFeOC was investigated at different doses at room temperature and 600°C. Crystallite amorphization and evolution were also studied at different doses at these temperatures. The underlying mechanisms of irradiation-induced microstructural changes in SiFeOC were discussed.

## 2. Experimental section

Commercial polysiloxane polyramic® SPR-684 (PSO) [-Si(C<sub>5</sub>H<sub>6</sub>)<sub>2</sub>O-]<sub>3</sub>(-Si(CH<sub>3</sub>)(H)O-)<sub>2</sub>(-Si(CH<sub>3</sub>)(CH=CH<sub>2</sub>)O-)<sub>2</sub>] was used as the C-rich polymer precursor (Starfire

Systems, Inc.). Octavinyl-polyhedral oligomeric silsesquioxane (POSS, OL1170) was supplied by Hybrid Plastics, Hattiesburg, MS. Platinum divinyltetramethyldisiloxane complex in xylene (2.1-2.4 %), a Pt Karstedt's reagent, was used as the catalyst (Gelest Inc., Morrisville, PA) for cross-linking.

In a typical experiment, 20 wt% POSS and 3 wt% Fe(acac)<sub>3</sub> relative to PSO were dissolved in a pentane solvent and then transferred to the PSO solution. These solutions were stirred at 500 rpm for 1 h along with 50 ppm of Pt catalyst to remove residual gas and homogenize the solution. The derived solution was degassed at 10 mTorr for 4 h and poured in cylindrical molds made from Al foil. Cross-linking was carried out in an oven for 48 h at 120°C. The cross-linked samples were polished and pyrolyzed in an Ar atmosphere at 1300°C with a heating rate of 1°C·min<sup>-1</sup>.

The phases present in the pyrolyzed coatings were characterized using an X'Pert PRO diffractometer with Cu K $\alpha$  radiation (PANalytical B.V., EA Almelo). Raman spectroscopy was carried out at 514 nm excitation using a Horiba spectrometer (JY, Horiba HR 800).

Sample liftouts with ~100 nm thickness were prepared using focused ion beam milling (FIB; Thermo Fisher Xe Plasma Helios 650). Kr ion irradiation experiments were performed in a 300 kV TEM (Thermo Fisher Tecnai G2 F30 TWIN) at the Michigan Ion Beam Laboratory (University of Michigan, Ann Arbor, MI, USA), where the ions travelled through a beamline (Beamline 6). The beamline was connected to a 400 kV ion implanter (Blue, National Electrostatics Corporation) equipped with an ion source (Model 921, Danfyzik, Denmark). The ion irradiation experiments were conducted with 1.2 MeV Kr ions at 25°C and 600°C at different fluences. At room temperatures, the damage levels were 1, 2, and 3 dpa. At 600°C, the damage levels were 2, 3, 4, 5, 8, 10, and 12 dpa. Scanning transmission electron microscopy (STEM) was used to examine the microstructure before, during, and after the irradiation.

### 3. Results and Discussion

#### 3.1. Phase and microstructure before irradiation

Fig. 1 shows the X-ray diffraction (XRD) pattern of the unirradiated SiFeOC ceramic. In the amorphous SiOC matrix, the dispersed crystalline phases include Fe<sub>3</sub>Si, SiC, and graphitic C. Recent studies revealed that POSS enhances PSO crosslinking because of its extensive vinylic terminal groups with a caged structure [22, 41]. The vinylic group improves the thermal stability of SiOC during the polymeric-to-ceramic conversion while the caged structure helps to attain more extensive nucleation of SiO<sub>2</sub> at temperatures as low as 1000°C [22, 41]. Under the catalytic effect of Fe, the crystalline phases include SiC, Fe<sub>3</sub>Si, and graphitic C. The peaks due to cubic β-SiC are observed at 35.2° (111 plane), 41.2° (200 plane), 59.9° (220 plane), and 71.9° (311 plane). The graphitic C phase is observed around 26.1° (002 plane) and 43.0° (101 plane). The SiO<sub>2</sub> peak centered around 23° is broad and reflects its amorphous nature. However, it overlaps with the 26.1° peak from graphitic C. Even though carbothermic reduction of FeO to Fe<sub>3</sub>Si via intermediate metastable Fe<sub>3</sub>C formation has been reported [24, 42], the cementite phase is unstable at >770°C in the presence of C. Thus, Fe<sub>3</sub>Si is the stable phase in this SiOC system. Two plausible reaction mechanisms can be suggested for the Fe<sub>3</sub>Si formation (eqns. 3-4) [24, 42]. Either Fe<sub>3</sub>C decomposes into metallic Fe and graphite to form Fe<sub>3</sub>Si, or Fe<sub>3</sub>C reacts with SiO<sub>2</sub> in the presence of graphite to form Fe<sub>3</sub>Si. The Gibbs free energy change at 1000°C for the former is -43.3 kJ·mol<sup>-1</sup> while for the latter it is -44.1 kJ·mol<sup>-1</sup>, which indicates that the latter is slightly more likely.



Therefore, use of the  $\text{Fe}(\text{acac})_3$  precursor in PSO helps the formation of  $\text{Fe}_3\text{Si}$  nanodomains.  $\text{FeO}$ ,  $\text{Fe}$ , and  $\text{Fe}_3\text{C}$  might have formed as intermediate phases. However, these phases are thermodynamically unstable and likely have undergone carbothermic reduction to form  $\text{Fe}_3\text{Si}$ , for which the XRD peaks are observed around  $45.2^\circ$  (220), and  $66.1^\circ$  (400),  $84.0^\circ$  (422) [43, 44].

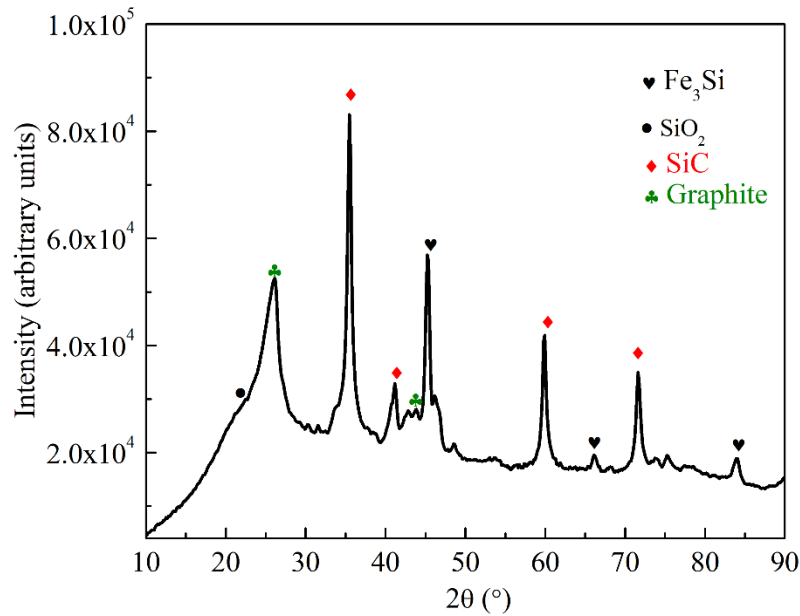


Fig. 1. XRD pattern of unirradiated SiFeOC ceramic showing the presence of amorphous  $\text{SiO}_2$ , graphitic C,  $\text{SiC}$ , and  $\text{Fe}_3\text{Si}$ .

Fig. 2 shows the Raman spectrum of the SiFeOC ceramic. Lorentzian fitting was carried out to deconvolute the peaks for D, G, 2D, and D+D' bands. The D and G bands centered around  $1324 \text{ cm}^{-1}$  and  $1598 \text{ cm}^{-1}$  confirm the presence of free C in the SiOC ceramic. The D mode centered around  $1324 \text{ cm}^{-1}$  corresponds to  $A_{1g}$  symmetry involving phonons of the K zone boundary, which is a forbidden mode in a perfect graphite system and can arise only in a disordered graphite system due to defects. The G mode centered around  $1598 \text{ cm}^{-1}$  has  $E_{2g}$  symmetry and is due to in-plane bond stretching vibration of  $\text{sp}^2$  C atoms. An overtone of the D mode appears around  $2658 \text{ cm}^{-1}$ . The Raman band appearing around

2967  $\text{cm}^{-1}$  is due to the D + D' band combination. The D' mode is similar to the D mode except that the phonon generation is from  $\Gamma$  point (from the electronic band structure of the graphite layers) [45].

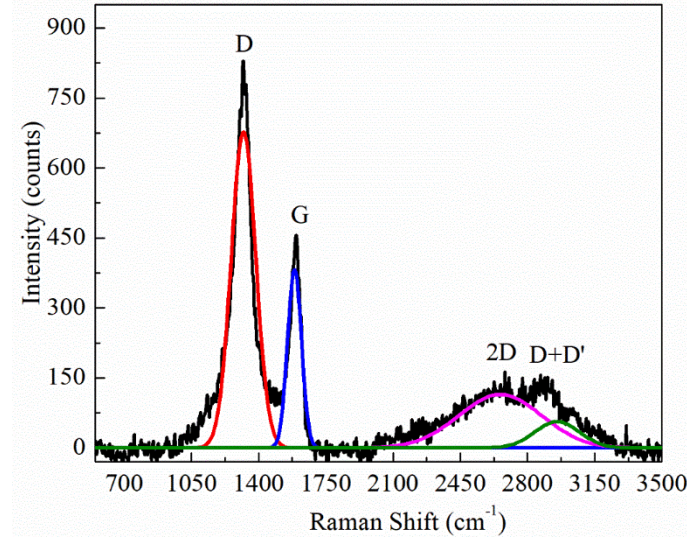


Fig. 2. Raman spectrum of unirradiated SiFeOC ceramic.

The integral intensity of the D and G bands can be used to calculate the degree of free C ordering ( $I_D/I_G$ ). The ratio of  $I_D/I_G$  for the SiFeOC ceramic is 3.12. This means that the disordered C concentration is higher than that of graphitic C. The free C cluster size can be calculated using the Tunistra and Koenig method [46]:

$$\frac{I_D}{I_G} = \frac{C(\lambda)}{L_a} \quad (5)$$

where  $I_D$  and  $I_G$  are the intensities of the D and G bands;  $C(\lambda)$  is a constant that depends on the wavelength of the incident beam.  $C(\lambda)$  is calculated using eqn. (6):

$$C(\lambda) = C_0 + \lambda C_1 \quad (6)$$

where  $C_0$  and  $C_1$  are -12.6 nm and 0.033 nm respectively,  $\lambda$  is the wavelength of the excitation source used (633 nm). The average C cluster size in SiFeOC is 2.66 nm.

Figs. 3a and b show the microstructure of the SiOC matrix with graphitic layers and ordered nanodomains. The corresponding SAED confirms the presence of crystalline  $\text{Fe}_3\text{Si}$

phase through crystallographic planes of (440) and (420) and the presence of SiC crystalline phase through crystallographic planes of (331) and (440). The crystallite phases are mostly <10 nm in size. The SiC phase forms due to Fe-accelerated carbothermal reduction. The exact reaction mechanisms are difficult to be distinguished due to the very close thermodynamic formation energy of Fe<sub>3</sub>Si from the two pathways discussed earlier (eqns. (3) and (4)).

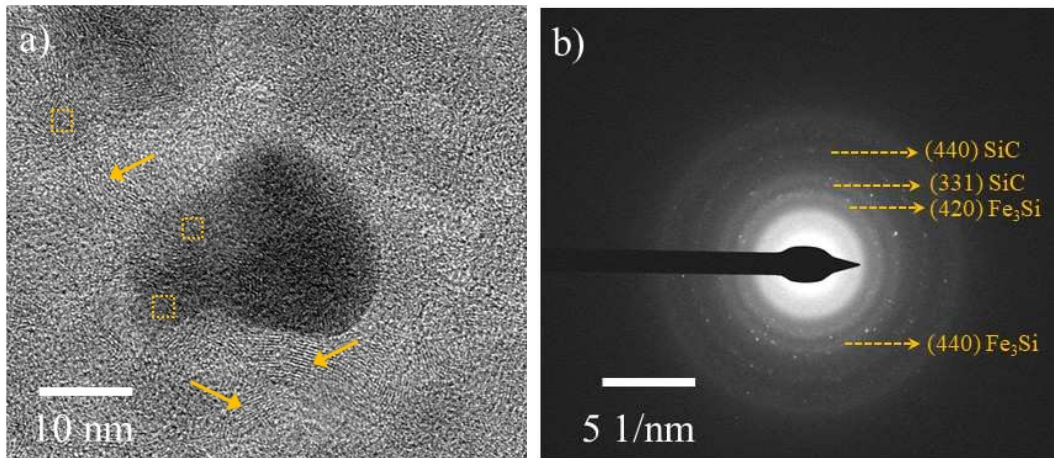


Fig. 3. (a) TEM image showing graphitic layers (yellow arrow) and nanocrystalline domains (yellow square), and (b) SAED pattern of unirradiated SiFeOC nanocomposite.

### 3.2. In-situ Kr irradiation effect at room temperature

Fig. 4 shows the TEM images of the SiFeOC nanocomposite at 3 dpa ion irradiation at room temperature. Lower dpa images show similar features and are omitted for brevity. The nanodomains with different contrast in Fig. 4a are from Fe<sub>3</sub>Si, SiO<sub>2</sub>, graphitic C, and SiC phases in the SiOC matrix. Their distribution is homogeneous, and their sizes are similar. The bright spots in Fig. 4b (dark field image) are from the Fe<sub>3</sub>Si and SiC phases, the higher atomic number and crystallinity lead to higher brightness. Due to the small sizes and wide range of contrast, it is impossible to quantify the size distributions of different nanodomains. Fig. 4c shows the enlarged nanodomains in the SiOC matrix, these nanodomains are most

likely  $\text{Fe}_3\text{Si}$  or  $\text{SiC}$  phases. There is a wide range of sizes, but these crystalline phases are in general  $<20$  nm. Because of the small sizes of these different domain regions and their homogeneous distribution in the  $\text{SiOC}$  matrix, there is a large amount of nanodomain- $\text{SiOC}$  matrix interfaces. Fig. 4d shows the high magnification of a selected zone from Fig. 4c. The nanodomain is around 20 nm and intimately embedded in the amorphous  $\text{SiOC}$  matrix without any pores or cracks or other kinds of defects.

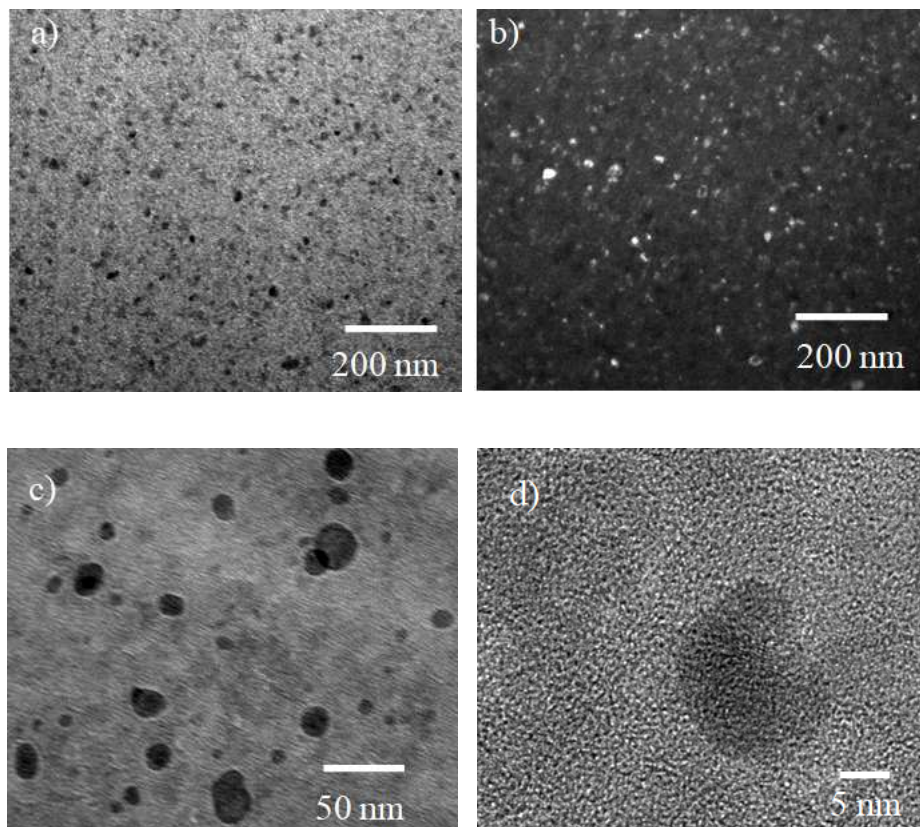


Fig. 4. TEM images of the  $\text{SiFeOC}$  nanocomposite after room temperature ion irradiation to 3 dpa: a) bright field image, b) dark field image, c) magnified image depicting the presence of different phases, and d) high resolution TEM image.

Fig. 5 shows the SAED patterns taken at different doses. At 0 dpa, both  $\text{Fe}_3\text{Si}$  and  $\text{SiC}$  nanocrystal domains are present. However, ion irradiation with 1 dpa results in the

disappearance of the diffraction spots from the (420) and (511) planes for Fe<sub>3</sub>Si and the disappearance of the diffraction spots from the (331), (440), and (622) planes for SiC. The diffraction spots observed at 1 dpa is due to either Fe<sub>3</sub>Si (440) or SiC (400) because the diffraction spots are very sparse and the computed “d” spacing is close to each other. Regardless, the disappearance of the diffraction spots from other planes indicates that the crystalline phases have partly amorphized. Increasing the irradiation dose to 2 dpa still shows partial amorphization but to a much larger extent (Fig. 5c). Diffraction spots due to Fe<sub>3</sub>Si or SiC are still visible. This means that the nanocrystal domains can sustain the ion irradiation up to 2 dpa. However, further increasing the irradiation dose to 3 dpa leads to complete amorphization of the crystalline phases, no diffraction spots or patterns are observed (Fig. 5d). At the end of the 3 dpa irradiation, the diffraction pattern only exhibits diffuse rings. The amorphization of SiC and Fe<sub>3</sub>Si nanodomains at such irradiation dose levels also provides data on the crystalline size effects on ion irradiation resistance compared to the bulk SiC [47, 48], which cannot provide such information due to its macroscopic size. Considering the <20 nm crystallite size, the nanodomains are very resistant to irradiation damage [47, 49, 50]. The small volume changes from the SiC and Fe<sub>3</sub>Si nanodomain amorphization also require low volume change and atomic structural adjustment from the SiOC matrix to accommodate swelling in addition to the fact that such atomic structural adjustment sites are widespread and readily available throughout the system. Thus, this SiFeOC nanocomposite can sustain the ion irradiation without defect formation/accumulation, swelling, or voids.

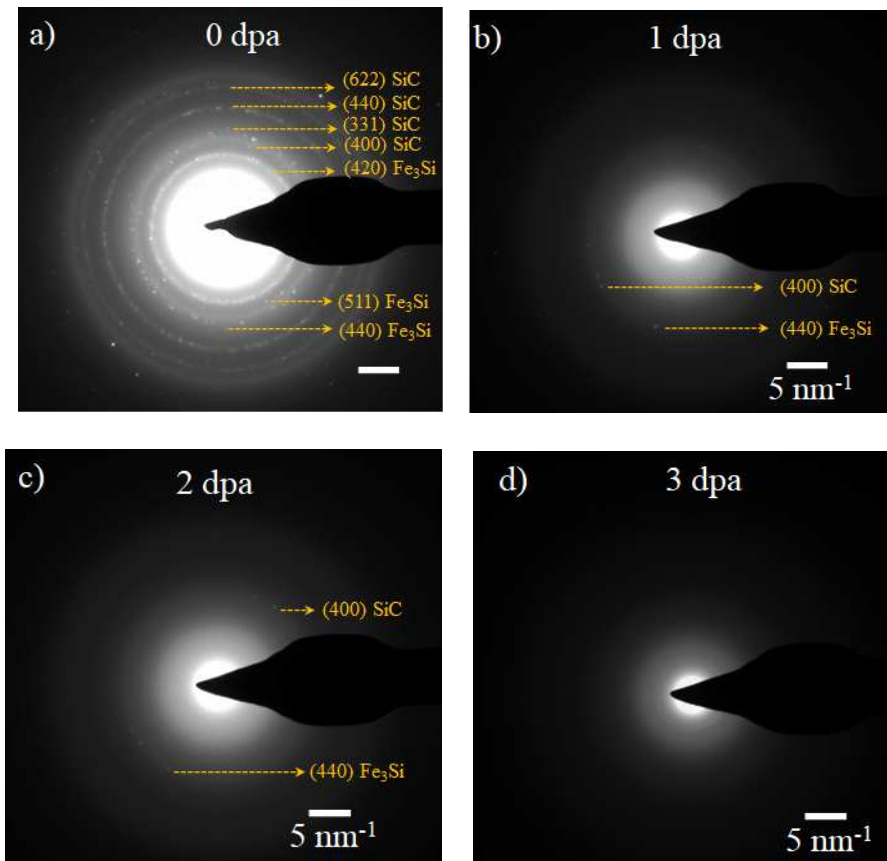


Fig. 5. SAED patterns of the SiFeOC ceramic at different ion irradiation doses at room temperature: (a) 0 dpa, (b) 1 dpa, (c) 2 dpa, and (d) 3 dpa.

As seen in Figs. 3 and 4, during irradiation, the amorphous and irradiation tolerant SiOC ceramic matrix separates different nanodomains (SiC, Fe<sub>3</sub>Si, and even turbostratic C) from each other [32]. For defects to diffuse and aggregate, they have to travel through the amorphous SiOC matrix. Moreover, the SiOC atomic structures are rigid and yet amorphous, which can remain stable while accommodating large strain and absorbing vacancies and diffusing species. The vacancies and interstitial species from the nanodomains of crystalline SiC, Fe<sub>3</sub>Si, and graphitic C can be accommodated by the amorphous SiOC. It has been claimed that the SiOC network forms voids much larger than the diameter of He atoms by connecting the SiO<sub>x</sub>C<sub>4-x</sub> tetrahedra in SiO<sub>2</sub>-rich and equiatomic specimens [51]. Even though

the size of Kr atoms (at 0.202 nm) is larger than that of He atoms (at 0.140 nm) by 0.06 nm, the accommodation of Kr and other migrating species is also possible through the voids in the SiOC amorphous structure. This is the so-called free volume accommodation. In the SiOCs with a higher amount of amorphous phases, changes in the amorphization degree of graphitic C are also smaller because the C content is lower and the SiOC matrix sustains more of the irradiation. The amorphous SiOC matrix can act as an efficient sink to accommodate the displaced atoms emitted from the crystalline phases [52]. Because of the above attributes, the SiFeOC composite exhibits good microstructural stability, conformal interface, and irradiation tolerance. Such effect is consistent with the report that SiO<sub>2</sub>-rich SiOC specimens show a greater radiation resistance than SiC-rich ones; the formation of He bubbles is highly suppressed in the SiO<sub>2</sub>-rich and equiatomic compositions after even 90 at% He implantation, whereas pronounced swelling occurs in the SiC-rich specimens. In this study, heavy Kr<sup>3+</sup> ion bombardment creates cascades and subcascades throughout the SiOC matrix [15]. The sp<sup>2</sup> C may absorb ion-induced kinetic energy and convert it into thermal spike, assisting in energy dissipation as thermal energy. Also, the dispersed graphitic C and amorphous C phases generate a large amount of interfaces, which can capture the displaced atoms induced by ion irradiation, thus reducing cascade collision damage [53]. From Figs. 4 and 5, it can be seen that even though the Fe<sub>3</sub>Si, graphitic C, and SiC phase nanodomains have amorphized under ion irradiation, their corresponding amorphous regions remain defect-free and form a continuous system with the SiOC matrix. These exceptional properties can also be attributed to the uniformly distributed nanoclusters and the strong bond between the nanoclusters and the SiOC matrix [54]. All these aspects demonstrate the high resistance of the SiFeOC system to ion irradiation and the strong capability for defect annihilation [13, 55]. Thus, the sample is devoid of pores, bubbles, or cracks.

### 3.3. High temperature irradiation

Fig. 6 shows the SAED patterns of the SiFeOC nanocomposite irradiated at different doses at 600°C. At 0 dpa (Fig. 6a), the diffraction rings show that the Fe<sub>3</sub>Si and SiC crystallites are stable at 600°C. This is as expected since the SiFeOC composite is pyrolyzed at 1300°C. Irradiation up to 2 dpa results in the disappearance of the diffraction spots from the (620) plane of SiC (Fig. 6b), indicating the lower stability of SiC under the Kr ion irradiation. However, the diffraction patterns corresponding to Fe<sub>3</sub>Si remain unchanged, confirming that the Fe<sub>3</sub>Si nanocrystalline domains are more stable against amorphization. At 3 dpa dose (Fig. S1a), the diffraction patterns corresponding to both Fe<sub>3</sub>Si and SiC are still present, confirming that Fe<sub>3</sub>Si and SiC have not undergone complete amorphization, unlike the sample irradiated at room temperature. Even at 4 dpa (Fig. S1b), no substantial change is observed.

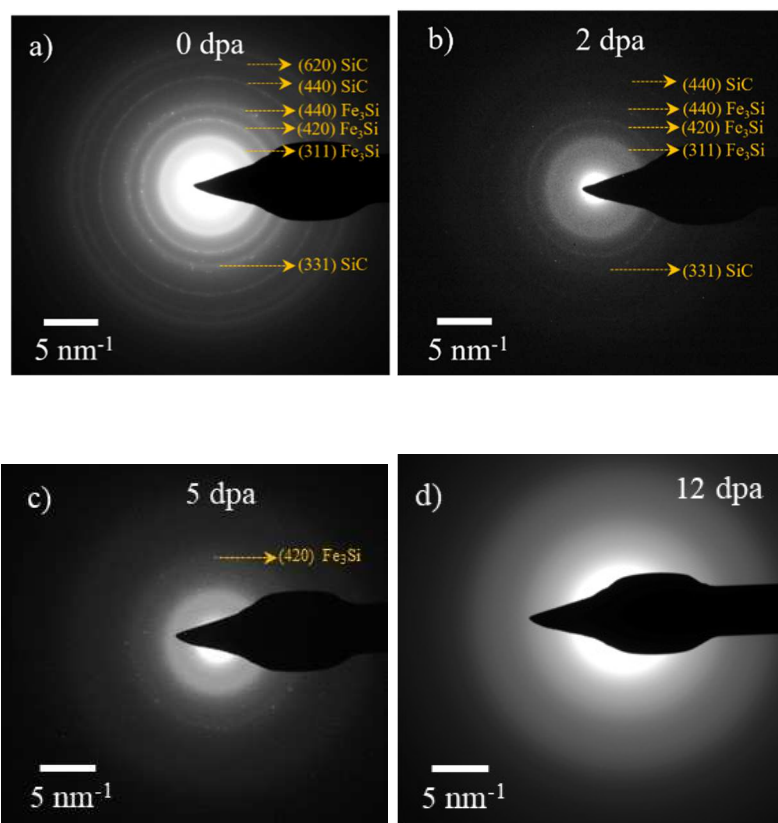


Fig. 6. SAED patterns of SiFeOC nanocomposite at different irradiation doses at 600°C: (a) 0 dpa, (b) 2 dpa, (c) 5 dpa, and (d) 12 dpa.

Comparing Figs. 5 and 6, it shows that high temperature Kr ion irradiation leads to less amorphization of the SiFeOC sample. This is because irradiation-induced amorphization results from two processes: creation of disorder or defects in crystalline solids by ion beam irradiation and preservation of defects due to constrained atomic or molecular movement [14]. At high temperatures, the ability to preserve defects decreases because of high kinetic energy and thus more atomic rearrangement to restore crystalline structure and minimize the total system energy. This is also claimed as defect annealing, damage mitigation, and crystalline structure recovery [47, 49]. The resulting stable phases are a balance between irradiated-induced damage buildup and dynamic annealing of defects at high temperatures [56]. Following a similar argument, this high temperature induced crystalline phase stability can be explained based on atomic level mixing and demixing. Based on a SiOC/crystalline Fe composite, two regimes of ion mixing have been proposed: one regime is independent of temperature due to ballistic mixing and the other regime is dependent on temperature and referred to as irradiation-enhanced demixing [57]. For low temperature irradiation where irradiation induced point defects cannot migrate, demixing between Fe and SiOC is the least for irradiation at low temperatures (e.g., 50 K) and accelerates as the irradiation temperature increases [15]. Similarly, higher temperature ion irradiation in this work, 600°C, leads to more de-mixing because SiOC and Fe<sub>3</sub>Si species are more mobile in order to re-store their crystalline order. Different crystalline phases are more likely to remain separate and resistant to atomic structural changes. Fig. 6 shows that the resistance to amorphization for the Fe<sub>3</sub>Si and SiC crystallites has significantly increased under 600°C ion irradiation, to 10 dpa (Fig. S1d) and 4 dpa (Fig. S1b), respectively. This can be attributed to the amorphization and demixing resistance increases with ion irradiation temperature increase.

With 5 dpa (Fig. 6c) and 8 dpa (Fig. S1c) irradiation, only Fe<sub>3</sub>Si nanocrystal domains remain while the SiC crystallites have amorphized. This means that Fe<sub>3</sub>Si is more stable than SiC, which has not been reported before. This is likely due to bond nature difference. For Fe<sub>3</sub>Si, the bonds between Fe and Si atoms are mainly ionic with some covalent bonding for Fe–Si [58]. For SiC, the bonds are largely covalent. After the breaking of the Fe–Si and Si–C bonds under the Kr ion irradiation, re-formation of the Si–C bond is difficult, if not impossible, due to bond directionality, while the Fe–Si bond can re-form more easily. The disappearance of the SiC nanodomains at 5 dpa sets its limit in ion irradiation resistance. As stated earlier, this ion irradiation resistance level is already high compared to bulk SiC irradiation resistance [47, 49, 50]. In Fig. 6d, the diffraction spots arising at 10 dpa still correspond to the (420) plane of Fe<sub>3</sub>Si, confirming the resiliency of Fe<sub>3</sub>Si to ion irradiation up to 10 dpa at 600°C (Fig. S1d). Further increase in the irradiation dose to 12 dpa (Fig. 6d) has resulted in complete amorphization of Fe<sub>3</sub>Si nanocrystalline domains. From this point forward, the stability of the SiFeOC ceramic can only arise from the structural accommodation of the amorphous SiOC matrix. More severe irradiation requires a higher degree of Si-containing tetrahedral accommodation in the amorphous SiOC matrix [53].

Fig. 7a shows the bright field image of the SiFeOC nanocomposite after irradiation at 600°C with 5 dpa (The images for the other dpa levels are similar as shown in Fig. S2). The entire sample is defect-free. There are no voids, bubbles, or cracks. Compared to Fig. 4a, the dark spots are more sparsely distributed with less contrast difference. This is because SiC has amorphized and the SiOC matrix only contains the Fe<sub>3</sub>Si phase. Because of the lower amount of the crystalline phase and the same species type, the dark phase can be more easily distinguished. Fig. 7a also indicates that the Fe<sub>3</sub>Si crystallites remain homogeneously dispersed. The dark field images (Figs. 7b and S3) consistently demonstrate such a trend. This kind of microstructures supports the earlier statement that irradiation-induced defects are

more mobile at elevated temperatures, which allows them to diffuse to defect sinks ( $\text{Fe}_3\text{Si}/\text{SiOC}$  interface or the SiOC matrix) to be annihilated, enhancing the stability of the SiFeOC nanocomposite system.

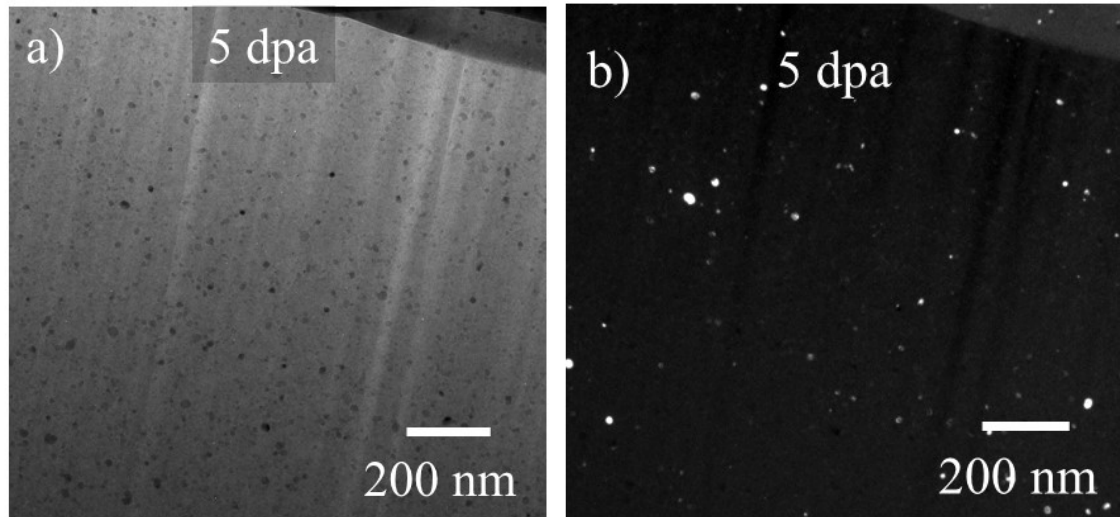
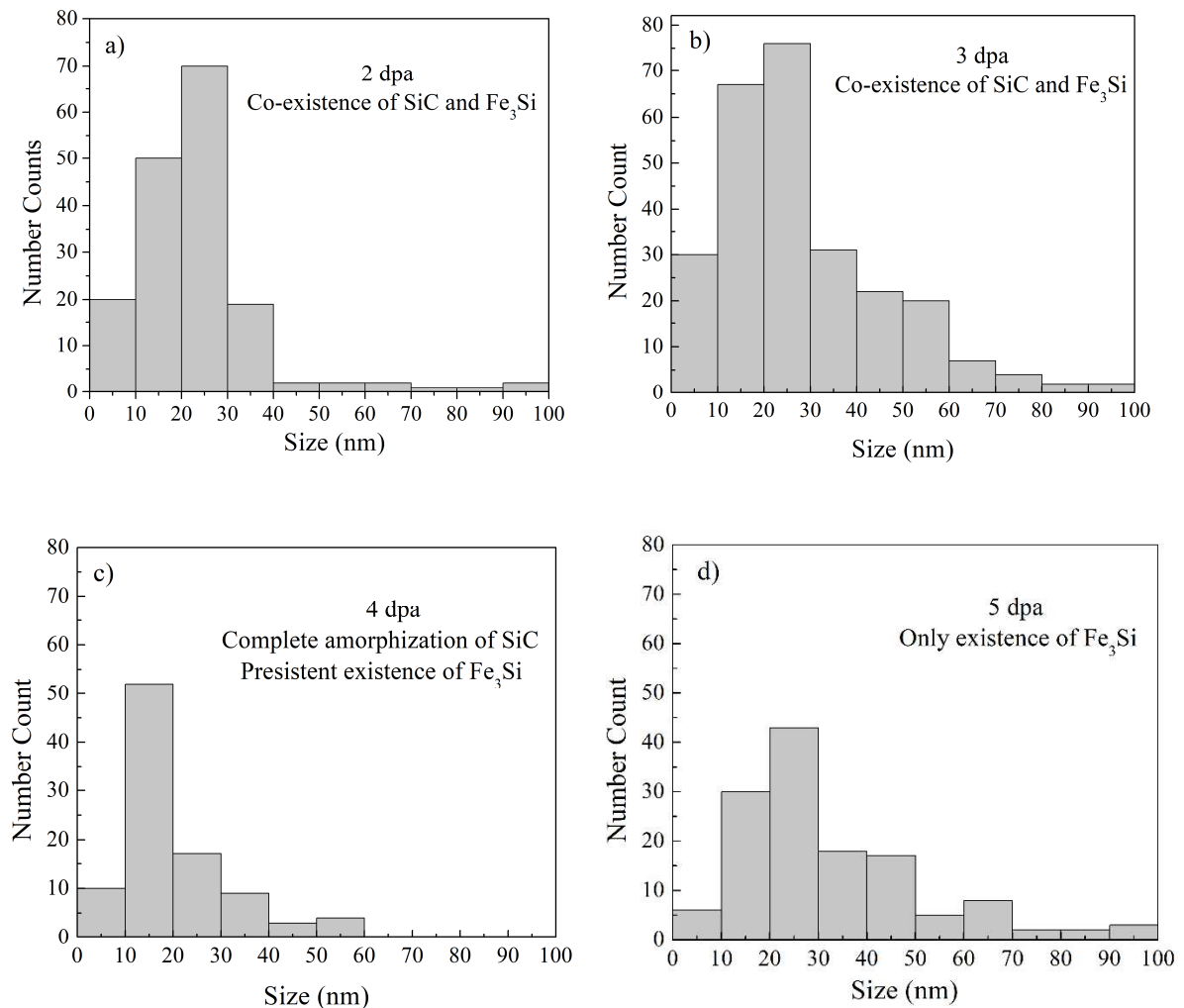


Fig. 7 (a) Bright field and (b) dark field images of the SiFeOC nanocomposite after 5 dpa irradiation at 600°C.

To evaluate the SiC/ $\text{Fe}_3\text{Si}$  crystallite size and distribution changes, the mean crystallite sizes were measured based on imaging contrast difference at each ion irradiation condition at 600°C and the results were plotted in Fig. 8. Due to the similarity in size and contrast, SiC and  $\text{Fe}_3\text{Si}$  crystallites cannot be distinguished. Regardless, the following observations can be made. From 2 dpa (Fig. 8a) to 3 dpa (Fig. 8b), the number of crystallites at less than 20 nm decreases while that at larger than 30 nm increases. Considering that SiC is being amorphized, the only explanation is that the  $\text{Fe}_3\text{Si}$  crystallite size has increased. At 4 dpa (Fig. 8c), there is an obvious decrease in crystallites at each size. This is likely due to the complete amorphization of the SiC crystallites (Fig. S1b). Consistently, the crystallite number count decreases and the size shifts to larger crystallites from 4 to 5 dpa, to 8 dpa, and to 10 dpa. This means that ion irradiation not only induces  $\text{Fe}_3\text{Si}$  amorphization but also  $\text{Fe}_3\text{Si}$

crystallite growth (consistent with the temperature-induced demixing statement earlier). As the  $\text{Fe}_3\text{Si}$  amorphization continues, the crystallite number count continuously decreases. The crystallite size increases due to the growth of larger crystallites at the expense of smaller crystallites. Eventually, these large  $\text{Fe}_3\text{Si}$  crystallites completely amorphize in the amorphous SiOC matrix, as shown in Fig. 6d. Such simultaneous  $\text{Fe}_3\text{Si}$  crystallite size increase and number decrease can only be observed at high temperatures in an amorphous matrix such as SiOC due to the prolonged presence of the  $\text{Fe}_3\text{Si}$  crystalline phase and the high temperature-induced demixing under ion irradiation.



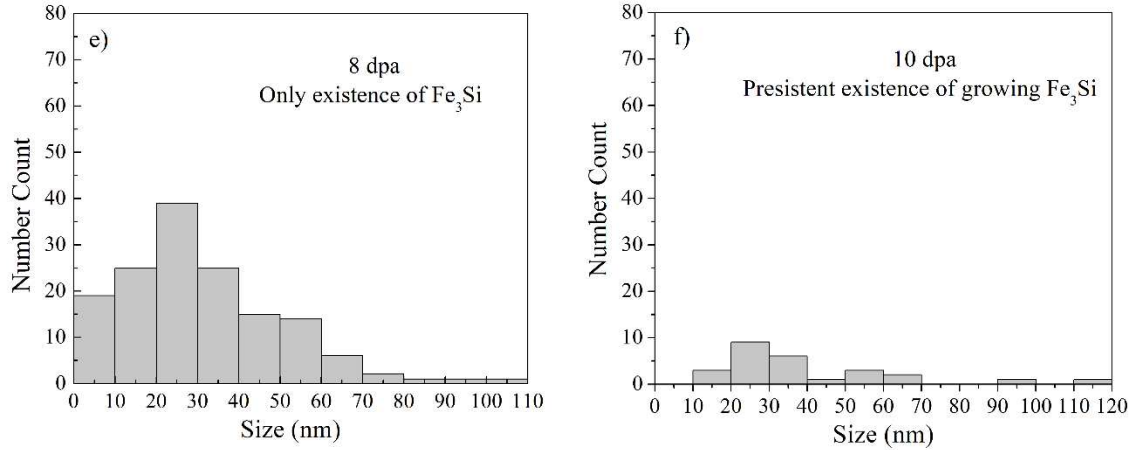


Fig. 8. Crystallite size distributions derived from in-situ TEM dark field images (given in Fig. 7 and Figs. S2 and S3) of the samples irradiated at 600°C: a) 2 dpa, b) 3 dpa, c) 4 dpa, d) 5 dpa, e) 8 dpa, and f) 10 dpa.

#### 4. Conclusions

For the first time, SiFeOC nanocomposite was studied at both room temperature and 600°C by in-situ Kr ion irradiation. Before ion irradiation, Fe<sub>3</sub>Si and SiC nanocrystallites uniformly distributed in the SiOC matrix. Room temperature ion irradiation showed that the nanocrystalline domains are stable up to 2 dpa and the crystallite-amorphous interface as well as the SiOC matrix act as defect sink sites. At 600°C, these nanocrystallites show increased stability. SiC crystals are stable up to 4 dpa while Fe<sub>3</sub>Si crystals are stable up to 10 dpa. With Kr ion irradiation at 600°C, the Fe<sub>3</sub>Si phase amorphizes while the remaining crystallite size increases and the number count decreases, ultimately leading to the complete amorphization of Fe<sub>3</sub>Si after 11 dpa. This SiFeOC composite is a promising irradiation resistant nuclear material for advanced gas cooled reactors.

## **Funding**

The Office of Nuclear Energy of Department of Energy (grant no. DE-NE0008807).

## **Declaration of interests**

The authors declare that they have no known competing financial interests or personal relationships that could have appeared to influence the work reported in this paper.

## **Declaration of Competing Interest**

The authors report no declarations of interest.

## **Acknowledgment**

This work was supported by the Office of Nuclear Energy of Department of Energy (grant No. DE-NE0008807). We acknowledge the experimental support from the Michigan Ion Beam Laboratory (University of Michigan) on the TEM work.

## **References:**

- [1] X.W. Zhou, C.H. Tang, Current status and future development of coated fuel particles for high temperature gas-cooled reactors, *Prog. Nuclear Energy*, 53(2) (2011) 182-188.
- [2] K. Minato, T. Ogawa, K. Sawa, A. Ishikawa, T. Tomita, S. Iida, H. Sekino, Irradiation experiment on ZrC-coated fuel particles for high-temperature gas-cooled reactors, *Nuclear Technol.*, 130(3) (2000) 272-281.
- [3] Q. Su, L. Price, J.A. Colon Santana, L. Shao, M. Nastasi, Irradiation tolerance of amorphous SiOC/crystalline Fe composite, *Mater. Lett.*, 155 (2015) 138-141.

- [4] X. Wang, H. Zhang, T. Baba, H. Jiang, C. Liu, Y. Guan, O. Elleuch, T. Kuech, D. Morgan, J.-C. Idrobo, P.M. Voyles, I. Szlufarska, Radiation-induced segregation in a ceramic, *Nat. Mater.*, 19(9) (2020) 992-998.
- [5] I.J. Beyerlein, M.J. Demkowicz, A. Misra, B.P. Uberuaga, Defect-interface interactions, *Prog. Mater. Sci.*, 74 (2015) 125-210.
- [6] A. Misra, M.J. Demkowicz, X. Zhang, R.G. Hoagland, The radiation damage tolerance of ultra-high strength nanolayered composites, *JOM* 59(9) (2007) 62-65.
- [7] E.G. Fu, A. Misra, H. Wang, L. Shao, X. Zhang, Interface enabled defects reduction in helium ion irradiated Cu/V nanolayers, *J. Nuclear Mater.*, 407(3) (2010) 178-188.
- [8] E.G. Fu, H. Wang, J. Carter, L. Shao, Y.Q. Wang, X. Zhang, Fluence-dependent radiation damage in helium (He) ion-irradiated Cu/V multilayers, *Phil. Mag.*, 93(8) (2013) 883-898.
- [9] N. Li, E.G. Fu, H. Wang, J.J. Carter, L. Shao, S.A. Maloy, A. Misra, X. Zhang, He ion irradiation damage in Fe/W nanolayer films, *J. Nuclear Mater.*, 389(2) (2009) 233-238.
- [10] R.E. Baumer, M.J. Demkowicz, Radiation response of amorphous metal alloys: Subcascades, thermal spikes and super-quenched zones, *Acta Mater.*, 83 (2015) 419-430.
- [11] Q. Su, S. Inoue, M. Ishimaru, J. Gigax, T. Wang, H. Ding, M.J. Demkowicz, L. Shao, M. Nastasi, Helium irradiation and implantation effects on the structure of amorphous silicon oxycarbide, *Sci. Rep.*, 7(1) (2017) 3900-3900.
- [12] M. Nastasi, Q. Su, L. Price, J.A. Colón Santana, T. Chen, R. Balerio, L. Shao, Superior radiation tolerant materials: Amorphous silicon oxycarbide, *J. Nuclear Mater.*, 461 (2015) 200-205.
- [13] Q. Su, L. Price, L. Shao, M. Nastasi, High temperature radiation responses of amorphous SiOC/crystalline Fe nanocomposite, *J. Nuclear Mater.*, 479 (2016) 411-417.

- [14] M. Nastasi, Q. Su, L. Price, J.A.C. Santana, T.Y. Chen, R. Balerio, L. Shao, Superior radiation tolerant materials: Amorphous silicon oxycarbide, *J. Nuclear Mater.*, 461 (2015) 200-205.
- [15] Q. Su, B. Cui, M.A. Kirk, M. Nastasi, In-situ observation of radiation damage in nano-structured amorphous SiOC/crystalline Fe composite, *Scr. Mater.*, 113 (2016) 79-83.
- [16] Q. Su, S. King, L.Y. Li, T.Y. Wang, J. Gigax, L. Shao, W.A. Lanford, M. Nastasi, Microstructure-mechanical properties correlation in irradiated amorphous SiOC, *Scr. Mater.*, 146 (2018) 316-320.
- [17] Z.H. Zhao, M. Niu, H.J. Wang, H.F. Gao, K. Peng, H. Zang, M.B. Ma, Preparation and the effects of ion irradiation on bulk SiOC ceramics, *J. Eur. Ceram. Soc.*, 39(4) (2019) 832-837.
- [18] N. Yang, K. Lu, Phase content prediction in polymer-derived ceramics with metal additives, *J. Am Ceram Soc.*, 104(10) (2021) 5379-5391.
- [19] N. Yang, C. Ophus, B.H. Savitzky, M.C. Scott, K. Bustillo, K. Lu, Nanoscale characterization of crystalline and amorphous phases in silicon oxycarbide ceramics using 4D-STEM, *Mater. Charact.*, 181 (2021) 111512.
- [20] K. Bawane, D. Erb, K. Lu, Carbon content and pyrolysis atmosphere effects on phase development in SiOC systems, *J. Eur. Ceram. Soc.*, 39(9) (2019) 2846-2854.
- [21] D. Erb, K. Lu, Additive and pyrolysis atmosphere effects on polysiloxane-derived porous SiOC ceramics, *J. Eur. Ceram. Soc.*, 37(15) (2017) 4547-4557.
- [22] D. Erb, K. Lu, Effect of additive structure and size on SiO<sub>2</sub> formation in polymer-derived SiOC ceramics, *J. Am. Ceram. Soc.*, 101(12) (2018) 5378-5388.
- [23] K. Lu, D. Erb, K. Bawane, N. Yang, Comparison of traditional and flash pyrolysis of different carbon content silicon oxycarbides, *J. Eur. Ceram. So.*, 39(10) (2019) 3035-3041.

- [24] M. Hojamberdiev, R.M. Prasad, C. Fasel, R. Riedel, E. Ionescu, Single-source-precursor synthesis of soft magnetic Fe<sub>3</sub>Si- and Fe<sub>5</sub>Si<sub>3</sub>-containing SiOC ceramic nanocomposites, *J. Eur. Ceram. Soc.*, 33(13) (2013) 2465-2472.
- [25] R. Mishra, R.K. Tiwari, A.K. Saxena, Synthesis of Fe–SiC nanowires via precursor route, *J. Inorg. Organometall. Polymer Mater.*, 19(2) (2009) 223-227.
- [26] L.X. Chen, J. Zhao, L. Wang, F. Peng, H. Liu, J.X. Zhang, J.W. Gu, Z.H. Guo, In-situ pyrolyzed polymethylsilsesquioxane multi-walled carbon nanotubes derived ceramic nanocomposites for electromagnetic wave absorption, *Ceram. Int.*, 45(9) (2019) 11756-11764.
- [27] A.V. Rau, K. Knott, K. Lu, Porous SiOC/SiC ceramics via an active-filler-catalyzed polymer-derived method, *Mater. Chem. Front.*, 5(17) (2021) 6530-6545.
- [28] N. Yang, K. Lu, Effects of transition metals on the evolution of polymer-derived SiOC ceramics, *Carbon* 171 (2021) 88-95.
- [29] C. Zhou, S.A. Li, Z.J. Yu, Polymer-derived Fe<sub>x</sub>Si<sub>y</sub>/SiC@SiOC ceramic nanocomposites with tunable microwave absorption behavior, *Int. J. Appl. Ceram. Technol.*, 19(2) (2022) 813-827.
- [30] A.V. Belevskii, I.E. Golubev, E.V. Klyukin, Z.S. Nikuradze, K.A. Pozdnyakov, M.V. Yudin, Prospective micro-encapsulated fuel with silicon carbide protective coat, *Atom. Energy*, 126(5) (2019) 279-285.
- [31] Q. Su, L. Price, J.A.C. Santana, L. Shao, M. Nastasi, Irradiation tolerance of amorphous SiOC/crystalline Fe composite, *Mater. Lett.*, 155 (2015) 138-141.
- [32] K.S. Ming, C. Gu, Q. Su, D.Y. Xie, Y.Q. Wu, Y.Q. Wang, L. Shao, M. Nastasi, J. Wang, Strength and plasticity of amorphous ceramics with self-patterned nano-heterogeneities, *Int. J. Plasticity*, 134 (2020).

- [33] X.L. Yan, F. Wang, K. Hattar, M. Nastasi, B. Cui, Novel amorphous SiOC dispersion-strengthened austenitic steels, *Materialia* 6 (2019).
- [34] Q. Su, H. Ding, L. Price, L. Shao, J.A. Hinks, G. Greaves, S.E. Donnelly, M.J. Demkowicz, M. Nastasi, Rapid and damage-free outgassing of implanted helium from amorphous silicon oxycarbide, *Sci. Rep.*, 8(1) (2018) 5009.
- [35] G.S. Was, Challenges to the use of ion irradiation for emulating reactor irradiation, *J. Mater. Res.*, 30(9) (2015) 1158-1182.
- [36] Q. Su, B. Cui, M.A. Kirk, M. Nastasi, Cascade effects on the irradiation stability of amorphous SiOC, *Phil. Mag. Lett.*, 96(2) (2016) 60-66.
- [37] A. Zare, Q. Su, J. Gigax, S.A. Shojaei, M. Nastasi, L. Shao, D.A. Lucca, Effects of ion irradiation on structural and mechanical properties of crystalline Fe/amorphous SiOC nanolaminates, *Acta Mater.*, 140 (2017) 10-19.
- [38] W. Yang, J. Pang, S. Zheng, J. Wang, X. Zhang, X. Ma, Interface effects on He ion irradiation in nanostructured materials, *Materials* 12(16) (2019) 2639.
- [39] X.H. Liu, J.Y. Huang, In situ TEM electrochemistry of anode materials in lithium ion batteries, *Energy Env. Sci.*, 4(10) (2011) 3844-3860.
- [40] M.L. Lescoat, J. Ribis, A. Gentils, O. Kaïtasov, Y. de Carlan, A. Legris, In situ TEM study of the stability of nano-oxides in ODS steels under ion-irradiation, *J. Nucl. Mater.*, 428(1) (2012) 176-182.
- [41] J. Li, K. Lu, T. Lin, F. Shen, Preparation of micro-/mesoporous SiOC bulk ceramics, *J. Am. Ceram. Soc.*, 98(6) (2015) 1753-1761.
- [42] E. Ionescu, C. Terzioglu, C. Linck, J. Kaspar, A. Navrotsky, R. Riedel, Thermodynamic control of phase composition and crystallization of metal-modified silicon oxycarbides, *J. Am. Ceram. Soc.*, 96(6) (2013) 1899-1903.

- [43] C.-B. Tang, H.-X. Chen, W. F.-R., X. N.-J., W. Hu, J.-Q. Xue, Facile preparation and tribological property of alloyed Fe<sub>3</sub>Si coatings on stainless steels surface by molten-salt infiltration method, *Surface Coating Technol.*, 397 (2020) 126049.
- [44] N. Borwornpornmetee, P. Charoenyuenyao, R. Chaleawpong, B. Paosawatyanong, R. Phatthanakun, P. Sittimart, K. Aramaki, T. Hamasaki, T. Yoshitake, N. Promros, Physical properties of Fe<sub>3</sub>Si films coated through facing targets sputtering after microwave plasma treatment, *Coatings* 11(8) (2021) 923.
- [45] A.C. Ferrari, J. Robertson, Interpretation of Raman spectra of disordered and amorphous carbon, *Phys. Rev. B*, 61(20) (2000) 14095-14107.
- [46] T. Jiang, Y. Wang, Y. Wang, N. Orlovskaya, L. An, Quantitative Raman analysis of free carbon in polymer-derived ceramics, *J. Am. Ceram. Soc.*, 92(10) (2009) 2455-2458.
- [47] A. Audren, A. Benyagoub, L. Thome, F. Garrido, Ion implantation of Cs into silicon carbide: Damage production and diffusion behaviour, *Nucl. Instrum. Meth. B* 257 (2007) 227-230.
- [48] W.J. Kim, S.M. Kang, K.H. Park, A. Kohyama, W.S. Ryu, J.Y. Park, Fabrication and ion irradiation characteristics of SiC-based ceramics for advanced nuclear energy systems, *J. Korean. Ceram. Soc.*, 42(8) (2005) 575-581.
- [49] N. Chaabane, M. Le Flem, M. Tanguy, S. Urvoy, C. Sandt, P. Dumas, Y. Serruys, Au ion irradiation of various silicon carbide fiber-reinforced SiC matrix composites, *J. Nucl. Mater.*, 439(1-3) (2013) 123-130.
- [50] Y.T. Yang, C.H. Zhang, C.H. Su, Z.N. Ding, Y. Song, Dose dependence of nano-hardness of 6H-SiC crystal under irradiation with inert gas ions, *Nucl. Instrum. Meth. B*, 422 (2018) 50-53.
- [51] S. Mizuguchi, S. Inoue, M. Ishimaru, Q. Su, M. Nastasi, Compositional effects on radiation tolerance of amorphous silicon oxycarbide, *J. Nucl. Mater.*, 518 (2019) 241-246.

- [52] M. Niu, H.F. Gao, Z.H. Zhao, H.J. Wang, L. Su, L. Zhuang, S.H. Jia, A. Navrotsky, Radiation effects in the crystalline-amorphous SiOC polymer-derived ceramics: Insights from experiments and molecular dynamics simulation, *ACS Appl. Mater. Inter.*, 13(33) (2021) 40106-40117.
- [53] M. Niu, H.J. Wang, H.F. Gao, Z.H. Zhao, L. Su, L. Zhuang, K. Peng, L. Xu, Effects of ion irradiation on microstructures and mechanical properties of SiOC nanocomposites, *J. Nucl. Mater.*, 558 (2022) 153383.
- [54] K.S. Ming, Q. Su, C. Gu, D.Y. Xie, Y.Q. Wang, M. Nastasi, J. Wang, Influence of metal additives on microstructure and properties of amorphous metal-SiOC composites, *JOM* 71(7) (2019) 2445-2451.
- [55] Q. Su, L. Price, L. Shao, M. Nastasi, Dose dependence of radiation damage in nanostructured amorphous SiOC/crystalline Fe composite, *Mater. Res. Lett.*, 4(1) (2016) 48-54.
- [56] B.Z. Su, H.Q. Liang, G.L. Liu, Z.R. Huang, X.J. Liu, Z.M. Chen, D.Y.W. Yu, Damage development of sintered SiC ceramics with the depth variation in Ar ion-irradiation at 600 degrees C, *J. Eur. Ceram. Soc.*, 38(5) (2018) 2289-2296.
- [57] Q. Su, F. Wang, B. Cui, M.A. Kirk, M. Nastasi, Temperature-dependent ion-beam mixing in amorphous SiOC/crystalline Fe composite, *Mater. Res. Lett.*, 4(4) (2016) 198-203.
- [58] Q. Zhang, G. Huang, S. Li, Mechanical properties of DO<sub>3</sub> based on First Principles, *Crystals* 10 (2020) 488.